294 *Chem. Mater.* **2010,** *22,* 294–304
DOI:10.1021/cm901821p

CHEMISTRY OF MATERIALS
Article

Photochemically Triggered Assembly of Composite Nanomaterials through the Photodimerization of Adsorbed Anthracene Derivatives

Anthony R. Smith and David F. Watson*

Department of Chemistry, University at Buffalo, The State University of New York, Buffalo, New York 14260-3000

Received June 26, 2009. Revised Manuscript Received November 18, 2009

Gold nanoparticles were assembled into three-dimensional aggregates in colloidal dispersions and were attached to ZrO_2 surfaces through photoinduced [4 + 4] cycloaddition reactions between adsorbed anthracene derivatives. Composite materials were characterized by ultraviolet/visible/near-IR spectroscopy, transmission electron microscopy, scanning electron microscopy, X-ray photoelectron spectroscopy, and time-of-flight secondary ion mass spectrometry (ToF-SIMS). Aggregates of gold nanoparticles with diameters of several micrometers were formed within 45 min of illumination at 355 nm and 130 mW/cm^2. Aggregation was attributed primarily to interfacial photodimerization between anthryl groups on different gold nanoparticles, although intramonolayer photodimerization reactions may also have occurred. 9-Anthracenethiolate-capped gold nanoparticles were attached to 2-anthroate-functionalized ZrO_2 surfaces upon excitation of anthryl $\pi-\pi^*$ transitions. ToF-SIMS data and the results of control experiments suggested that the materials assembly mechanism involved [4 + 4] cycloaddition reactions between adsorbed anthryl groups on gold and ZrO_2. Patterned arrays of nanoparticles with ~100-μm features were deposited onto surfaces. The use of interfacial photodimerization reactions to trigger materials assembly processes may represent an attractive materials fabrication strategy, in which photopatterning (top-down) and nanoparticle-adsorption (bottom-up) processes proceed via a single photoinduced reaction.

Introduction

The externally triggered organization of nanometer-scale components into ordered assemblies may enable the fabrication of complex nanostructures with tunable properties and reactivity. Materials assembly processes have been initiated by various stimuli, including changes of solvent polarity,[1,2] temperature,[3] oxidation state,[4] the concentration of solutes,[5−10] and the color and intensity of incident light.[11−19] Photochemically triggered assembly is advantageous for certain applications, because it enables both temporal and spatial control over the formation of nanostructures. Light is easy to generate and focus, and photochemical reactions are initiated only during the excited-state lifetime of the chromophore and within the illuminated volume of a reaction mixture or area of a surface.

Several methods have been reported for the photochemically triggered assembly of nanoparticles, both on surfaces and within colloidal dispersions. Assembly on surfaces has been achieved by the photolithographic patterning of thin films of nanoparticles.[20,21] Photochemical cleavage or cross-linking of capping groups induces changes in the surface polarity or solubility of nanoparticles, enabling the localization of nanoparticles on surfaces. A related method involves

(1) Ionov, L.; Sapra, S.; Synytska, A.; Rogach, A. L.; Stamm, M.; Diez, S. *Adv. Mater.* **2006**, *18*, 1453–1457.
(2) Gupta, S.; Agrawal, M.; Uhlmann, P.; Simon, F.; Oertel, U.; Stamm, M. *Macromolecules* **2008**, *41*, 8152–8158.
(3) Hu, Y.; Mei, T.; Guo, J.; White, T. *Inorg. Chem.* **2007**, *46*, 11031–11035.
(4) Ling, X. Y.; Reinhoudt, D. N.; Huskens, J. *Chem. Mater.* **2008**, *20*, 3574–3578.
(5) Mirkin, C. A.; Letsinger, R. L.; Mucic, R. C.; Storhoff, J. J. *Nature* **1996**, *382*, 607–609.
(6) Alivisatos, A. P.; Johnsson, K. P.; Peng, X.; Wilson, T. E.; Loweth, C. J.; Bruchez, M. P., Jr.; Schultz, P. G. *Nature* **1996**, *382*, 609–611.
(7) Tokareva, I.; Minko, S.; Fendler, J. H.; Hutter, E. *J. Am. Chem. Soc.* **2004**, *126*, 15950–15951.
(8) Liu, J.; Lu, Y. *J. Am. Chem. Soc.* **2005**, *127*, 12677–12683.
(9) Wu, L.-Q.; Lee, K.; Wang, X.; English, D. S.; Losert, W.; Payne, G. F. *Langmuir* **2005**, *21*, 3641–3646.
(10) Gupta, S.; Uhlmann, P.; Agrawal, M.; Chapuis, S.; Oertel, U.; Stamm, M. *Macromolecules* **2008**, *41*, 2874–2879.
(11) Ueda, M.; Kim, H.-B.; Ichimura, K. *J. Mater. Chem.* **1994**, *4*, 883–889.
(12) Ueda, M.; Fukushima, N.; Kudo, K.; Ichimura, K. *J. Mater. Chem.* **1997**, *7*, 641–645.
(13) Manna, A.; Chen, P.-L.; Akiyama, H.; Wei, T.-X.; Tamada, K.; Knoll, W. *Chem. Mater.* **2003**, *15*, 20–28.
(14) Bell, N. S.; Piech, M. *Langmuir* **2006**, *22*, 1420–1427.
(15) Zhou, J.; Sedev, R.; Beattie, D.; Ralston, J. *Langmuir* **2008**, *24*, 4506–4511.
(16) Sidhaye, D. S.; Kashyap, S.; Sastry, M.; Hotha, S.; Prasad, B. L. V. *Langmuir* **2005**, *21*, 7979–7984.
(17) Fava, D.; Winnik, M. A.; Kumacheva, E. *Chem. Commun.* **2009**, 2571–2573.
(18) Itoh, H.; Tahara, A.; Naka, K.; Chujo, Y. *Langmuir* **2004**, *20*, 1972–1976.
(19) Huh, S.; Chae, B.; Kim, S. B. *J. Colloid Interface Sci.* **2008**, *327*, 211–215.
(20) Jun, S.; Jang, E.; Park, J.; Kim, J. *Langmuir* **2006**, *22*, 2407–2410.
(21) Kim, W. J.; Kim, S. J.; Lee, K.-S.; Samoc, M.; Cartwright, A. N.; Prasad, P. N. *Nano Lett.* **2008**, *8*, 3262–3265.

Published on Web 12/28/2009

the photolithographic patterning of self-assembled monolayers on substrate surfaces. Photochemical degradation or modification of adsorbates yields patterned monolayers, which have been used as templates for the site-selective adsorption of nanoparticles.[22−27]

Photochemically triggered assembly of dispersed gold nanoparticles has been achieved through excitation of either the surface plasmon resonance or interband transitions, leading to aggregation, flocculation of colloids, and deposition of nanoparticles onto surfaces.[28−34] Aggregation may be driven by optical forces, or enhanced dispersion interactions between nanoparticles induced by excitation of the surface plasmon.[28−31,35,36] Alternatively, excitation of interband transitions may initiate electron transfer reactions that alter surface charges, leading to aggregation.[30,33,34] The light-triggered organization of dispersed nanoparticles into three-dimensional assemblies has also been achieved through photothermal processes. For example, localized temperature gradients created by the excitation of surface plasmon resonances of gold nanorods were used to modify adsorbed capping groups, leading to self-assembly of the nanorods.[17]

The photochemical assembly of dispersed nanoparticles triggered by reactions of photoactive capping groups has also been reported. The photoinduced isomerization or intramonolayer dimerization of adsorbates can alter the surface polarity of suspended nanoparticles, leading to aggregation of nanoparticles or sedimentation of colloidal dispersions.[11−15] Similarly, photoisomerization of adsorbates was used to control the interparticle spacing within aggregated assemblies of gold nanoparticles.[16] In an alternative approach, photodimerization reactions between capping groups on *different* nanoparticles, herein referred to as interfacial photodimerization reactions, have been used to trigger aggregation within colloidal dispersions.[18,19] Interfacial photodimerization yields covalent linkages between nanoparticles, potentially enabling control over the distance and electronic coupling between nanoparticles within assemblies. Furthermore, interfacial photodimerization may enable the site-selective attachment of nanoparticles to monolayer-functionalized substrate surfaces in a single step, rather than in a two-step process involving photopatterning followed by bottom-up assembly.

Scheme 1. Schematic Representation of Targeted Photodimerization-Induced Materials Assembly Processes[a]

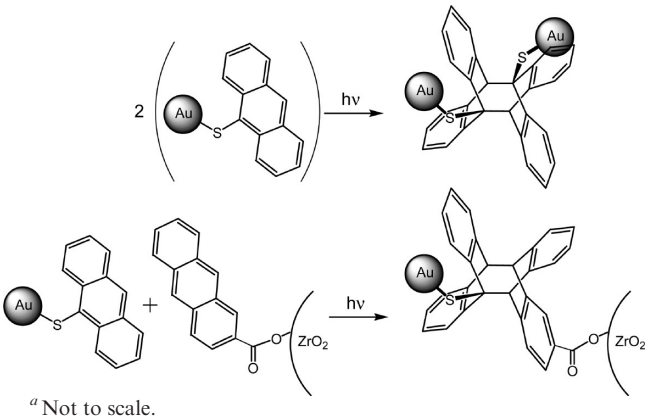

[a] Not to scale.

In this article, we report the use of interfacial photodimerization reactions between adsorbed anthracene derivatives to trigger the aggregation of gold nanoparticles in suspension and the attachment of gold nanoparticles to surfaces. The photodimerization chemistry of anthracene is well established.[37,38] In solution, anthracene exhibits vibrationally spaced $\pi-\pi^*$ bands centered at approximately 360 nm. Illumination into these bands leads to dimerization through [4 + 4] cycloaddition at the 9 and 10 positions with a quantum yield of approximately 0.3.[38] Anthracene dimers can be dissociated photochemically by illuminating at wavelengths from 250 to 290 nm or thermally by heating to approximately 250−340 °C.[38,39] The reversible photocyclization reactivity of anthracene may be particularly useful for materials fabrication, as it potentially enables the controlled assembly *and* disassembly of nanostructured entities. Indeed, the photodimerization of anthracene has been applied in the reversible formation of organic oligomers and polymers.[40] Importantly, photodimerization reactions between anthryl moieties of adsorbates within self-assembled monolayers have been shown to proceed efficiently.[39,41] Intramonolayer photodimerization reactions between adsorbed anthracene derivatives were recently exploited in the design of molecular switches involving photochemically modulated host−guest chemistry.[42]

The research reported in this article establishes the use of interfacial photodimerization reactions between anthryl moieties to trigger the assembly of inorganic nanoparticles into composite entities. We focus first on the photoinduced aggregation of anthracenethiolate-capped

(22) Liu, J.-F.; Zhang, L.-G.; Gu, N.; Ren, J.-Y.; Wu, Y.-P.; Lu, Z.-H.; Mao, P.-S.; Chen, D.-Y. *Thin Solid Films* **1998**, *327−329*, 176–179.
(23) Ryan, D.; Nagle, L.; Fitzmaurice, D. *Nano Lett*. **2004**, *4*, 573–575.
(24) del Campo, A.; Boos, D.; Spiess, H. W.; Jonas, U. *Angew. Chem., Int. Ed*. **2005**, *44*, 4707–4712.
(25) Riskin, M.; Katz, E.; Gutkin, V.; Willner, I. *Langmuir* **2006**, *22*, 10483–10489.
(26) Riskin, M.; Gutkin, V.; Felner, I.; Willner, I. *Angew. Chem., Int. Ed*. **2008**, *47*, 4416–4420.
(27) Dibbell, R. S.; Soja, G. R.; Hoth, R. M.; Watson, D. F. *Langmuir* **2007**, *23*, 3432–3439.
(28) Eckstein, H.; Kreibig, U. *Z. Phys. D: At., Mol. Clusters* **1993**, *26*, 239–241.
(29) Satoh, N.; Hasegawa, H.; Tsujii, K.; Kimura, K. *J. Phys. Chem.* **1994**, *98*, 2143–2147.
(30) Takeuchi, Y.; Ida, T.; Kimura, K. *J. Phys. Chem. B* **1997**, *101*, 1322–1327.
(31) Murakoshi, K.; Nakato, Y. *Adv. Mater*. **2000**, *12*, 791–795.
(32) Niidome, Y.; Hori, A.; Takahashi, H.; Goto, Y.; Yamada, S. *Nano Lett*. **2001**, *2001*, 365–369.
(33) Busby, M.; Scandola, F. *Chem. Commun*. **2006**, 4324–4326.
(34) Werner, D.; Hashimoto, S.; Tomita, T.; Matsuo, S.; Makita, Y. *J. Phys. Chem. C* **2008**, *112*, 16801–16808.
(35) Kimura, K. *J. Phys. Chem*. **1994**, *98*, 11997–12002.
(36) Hallock, A. J.; Redmond, P. L.; Brus, L. E. *Proc. Natl. Acad. Sci. U. S. A*. **2005**, *102*, 1280–1284.
(37) Bouas-Laurent, H.; Castellan, A.; Desvergne, J.-P.; Lapouyade, R. *Chem. Soc. Rev*. **2000**, *29*, 43–55.
(38) Bouas-Laurent, H.; Castellan, A.; Desvergne, J.-P.; Lapouyade, R. *Chem. Soc. Rev*. **2001**, *30*, 248–263.
(39) Fox, M. A.; Wooten, M. D. *Langmuir* **1997**, *13*, 7099–7105.
(40) Ikegami, M.; Onshiro, I.; Arai, T. *Chem. Commun*. **2003**, 1566–1567.
(41) Zareie, M. H.; Barber, J.; McDonagh, A. M. *J. Phys. Chem. B* **2006**, *110*, 15951–15954.
(42) Schäfer, C.; Eckel, R.; Ros, R.; Mattay, J.; Anselmetti, D. *J. Am. Chem. Soc*. **2007**, *129*, 1488–1489.

gold nanoparticles in suspension. We then report the attachment of anthracenethiolate-capped gold nanoparticles to anthroate-functionalized nanocrystalline ZrO_2 films. The targeted materials assembly processes are outlined qualitatively in Scheme 1.

Experimental Section

Materials and Instrumentation. Anthracene, 9-anthroic acid, 9-bromoanthracene, octanethiol, and poly(ethyleneglycol) were obtained from Aldrich. Hydrogen tetrachloroaurate(III), tetra-*n*-octylammonium bromide (TOAB), and zirconium(IV) tetraisopropoxide (isopropanol adduct) were obtained from Alfa Aesar. 2-Anthroic acid was obtained from TCI America. Sodium ethanethiolate was obtained from Fluka. Other common chemicals were obtained through various commercial sources. All reagents were used as received. Ultraviolet/visible/near-IR (UV/vis/NIR) absorption spectra were obtained using an Agilent 8453 spectrophotometer. Fourier transform infrared (FTIR) spectra were acquired with a Perkin-Elmer 1760X FTIR spectrophotometer with 2 cm^{-1} resolution. Gas chromatography−mass spectrometry (GC-MS) was performed using a Hewlett-Packard 5890 Series II gas chromatograph connected to a Hewlett-Packard 5972 Series mass selective detector. Scanning electron microscopy (SEM) images were acquired using a Hitachi S-4000 instrument (to determine film thickness) and a Hitachi SU70 thermally assisted field emission SEM with an SE(U) detector (to determine particle size). Transmission electron microscopy (TEM) images were acquired using a JEOL JEM 100 CX instrument. Digital image scans were analyzed using ImageJ software. X-ray photoelectron spectroscopy (XPS) spectra were obtained by SSI Small Spot ESCA with a monochromatic Al Kα X-ray source. Survey spectra revealed minimal contamination. High-resolution spectra were acquired for the S 2p, C 1s, and O 1s regions. The binding energy scales were calibrated to the aliphatic hydrocarbon C 1s peak at 284.6 eV. Samples were prepared by evaporating illuminated and unilluminated toluene dispersions of 9-anthracenethiolate-capped gold nanoparticles to dryness onto glass slides heated to 100 °C. Short integration times were used to minimize degradation of samples. Digital photographs of ZrO_2 films were taken with an Olympus FE-210 7.1 megapixel hand-held digital camera.

Time-of-flight Secondary Ion Mass Spectrometry (ToF-SIMS). ToF-SIMS analysis was performed on an ION TOF 5.100 ION TOF Gmbh (Muenster, Germany). 25-kV Bi_3^{+2} primary ions were used for image acquisition of low mass species, whereas 10-kV Cs^+ primary ions were used to increase the relative yield of the molecular ions versus high-mass substrate clusters for spectral comparison. Negative secondary ions were collected and accelerated to 2 kV and mass analyzed in a reflectron-type time-of-flight tube. The reflectron voltage was adjusted to compensate for different surface potentials of the samples. A low energy (20 V) electron flood gun was utilized for charge compensation. Ions were postaccelerated to 10 kV and detected with a multichannel plate detector. Spectra were analyzed with IONSPEC software; images were analyzed with IONIMAGE software (version 4.1.0.1).

Synthesis of 9-Anthracenethiol. 9-Anthracenethiol was synthesized from 9-bromoanthracene by adaptation of the method described by Testaferri et al.[43] for the thiolation of unactivated aryl halides. A 100-mL round-bottom flask was charged with 9-bromoanthracene (0.25 g, 1.0 mmol) and sodium ethanethiolate (0.7 g, 8.3 mmol). *N*,*N*-Dimethylformamide (DMF) (5 mL) was added, and the reaction was refluxed overnight under argon. Once the reaction cooled and the DMF was removed under vacuum, hydrochloric acid (20 mL, 0.1 M) was added under vigorous stirring. The organic product was extracted with dichloromethane, rinsed three times with distilled water, and dried over anhydrous sodium sulfate. The product was analyzed by GC-MS (Figure S1 of the Supporting Information). The molecular-ion peak was present at m/z 210, corresponding to anthracenethiol, and the isotopic distribution was appropriate.

Synthesis of Gold Nanoparticles Capped with 9-Anthracenethiolate or Octanethiolate. The synthesis of gold nanoparticles followed the method of Brust et al.[44−48] An aqueous solution of hydrogen tetrachloroaurate(III) (10 mL, 30 mM) was added to a toluene solution of TOAB (20 mL, 50 mM). The mixture was stirred vigorously for 30 min. The resulting emulsion, consisting of a dark orange organic layer and a colorless aqueous layer, was reduced by slowly adding a freshly prepared aqueous solution of sodium borohydride (30 mL, 0.3 M). The resulting reddish purple suspension was stirred for 30 min prior to the removal of the aqueous layer and subsequent rinsing with distilled water. Toluene suspensions of gold nanoparticles exhibited an absorption band at ∼530 nm, corresponding to the gold plasmon band. TEM images revealed particles with average diameters of (15 ± 7) nm. Organic thiols were adsorbed to the gold nanoparticles by adding the thiol to the organic layer containing the phase-transferred gold complex (in a 3:1 ratio to gold)[49] before reducing with sodium borohydride. Suspensions were rinsed with appropriate solvents prior to use.

Synthesis and Surface Functionalization of Nanocrystalline ZrO_2 Films. Nanocrystalline ZrO_2 films were prepared by adaptation of the method reported by Heimer et al.[50] Zirconium(IV) tetraisopropoxide (50 mL) was added slowly to rapidly stirred dilute nitric acid (300 mL, 0.5% v/v), which was purged with nitrogen. The resulting mixture was boiled until the total volume was reduced to 90 mL. The reaction mixture was then heated at 200 °C in a sealed vessel for 15 h, after which polyethylene glycol (5.4 g) was added and the mixture was stirred for an additional 8 h. Films were prepared by spreading this mixture onto glass slides then annealing in air (430 °C, 30 min). Anthroic acids were adsorbed to ZrO_2 by immersing the films in freshly prepared solutions of the acid in THF. For photochemical experiments, 15-mM solutions of anthroic acids were used. After a minimum of 4 h, films were removed from adsorption solutions and rinsed with the adsorption solvent. Films were stored in the dark until characterization by UV−vis spectroscopy and use in photochemical experiments. ZrO_2 powders for IR spectroscopy were prepared by scraping films from the glass substrate.

Photochemically Triggered Materials Assembly. Two light sources were used to trigger materials assembly processes. Lower-intensity light at 385 nm was generated by a Xe arc lamp

(43) Testaferri, L. T.; Tingoli, M.; Chianelli, D.; Montanucci, M. *Synthesis* **1993**, *9*, 5319–5324.

(44) Fink, J.; Kiely, C. J.; Bethell, D.; Schiffrin, D. J. *Chem. Mater.* **1998**, *10*, 922–926.
(45) Leff, D. V.; Brandt, L.; Heath, J. R. *Langmuir* **1996**, *12*, 4723–4730.
(46) Lu, A. H.; Lu, G. H.; Kessinger, A. M.; Foss, C. A., Jr. *J. Phys. Chem. B* **1997**, *101*, 9139–9142.
(47) Brust, M.; Bethell, D.; Kiely, C. J.; Schiffrin, D. J. *Langmuir* **1998**, *14*, 5425–5429.
(48) Brust, M.; Walker, M.; Bethell, D.; Schiffrin, D. J.; Whyman, R. *J. Chem. Soc., Chem. Commun.* **1994**, *7*, 801–802.
(49) Badia, A.; Cuccia, L.; Demers, L.; Morin, F.; Lennox, R. B. *J. Am. Chem. Soc.* **1997**, *119*, 2682–2692.
(50) Heimer, T. A.; D'Arcangelis, S. T.; Farzad, F.; Stipkala, J. M.; Meyer, G. J. *Inorg. Chem.* **1996**, *35*, 5319–5324.

(Oriel Photomax) output through a monochromator (Newport Cornerstone 260 1/4 m). Higher-intensity light at 355 nm was generated by a frequency-tripled Continuum Powerlite Precision II 8000 Nd:YAG laser (6−8 nm pulse width, 10 Hz repetition rate, 50−150 mW/cm^2). Solution-phase reactions took place in capped quartz cuvets. Excitation wavelengths of 385 and 355 nm were used. Reactions were monitored by UV/vis/NIR spectroscopy. Reactions on ZrO_2 surfaces were performed by immersing anthroate-functionalized ZrO_2 films on glass slides in the appropriate solvent or suspension within 1-cm quartz cuvets, such that the film faced away from the light source. Films were illuminated at 355 nm at various intensities. Micropatterned ZrO_2 films were prepared using a 1951 USAF chromium-on-glass resolution target (Edmund Optics) as a photomask. To minimize diffraction, the photomask was placed flush between the wall of the cuvet and the glass substrate under the ZrO_2 film.

Results and Discussion

Photochemically Triggered Assembly of Dispersed Gold Nanoparticles. The aggregation of 9-anthracenethiolate-capped gold nanoparticles was chosen for initial experiments to explore the photodimerization-induced assembly of dispersed nanoparticles. The aggregation of gold colloids gives rise to dramatic color changes, enabling facile characterization of materials assembly processes by absorption spectroscopy. The plasmon band of gold colloids is typically centered near 525 nm. Upon aggregation, as the distance between gold nanoparticles decreases below the average particle diameter, the band is red-shifted significantly and broadened.[51−53] As a result of these spectral changes, the color of gold colloids changes from red to blue.[5] Changes of color and absorption spectra have been used to characterize the pH-induced flocculation of gold colloids[54,55] and the assembly of gold nanoparticles through either covalent linkages or biomolecular recognition reactions between adsorbed capping groups.[5,56−61]

In our experiments, colloidal dispersions of 9-anthracenethiolate-capped gold nanoparticles in toluene were illuminated at 385 nm. UV/vis/NIR absorption spectra of the colloids were acquired as a function of time (Figure 1). Initial experiments were performed at low light intensity (410 μW/cm^2) and with low concentrations of gold nanoparticles. Illumination caused a decrease of the intensity

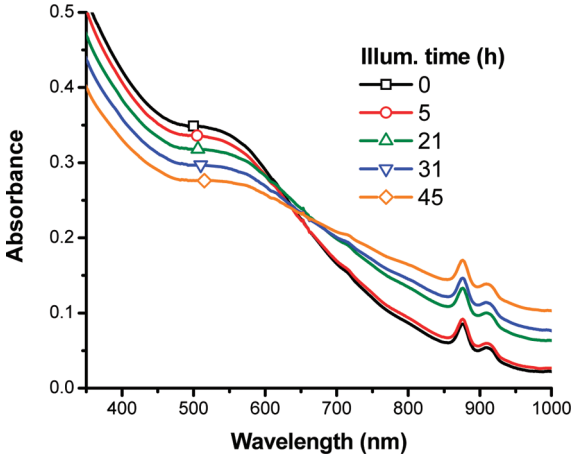

Figure 1. UV/vis/NIR absorption spectra of toluene suspensions of 9-anthracenethiolate-capped gold nanoparticles as a function of illumination time at 385 nm and 410 μW/cm^2. (The peaks at 876 and 911 nm are artifactual.)

of the plasmon band and the growth of a broad absorption beyond 640 nm, indicating that gold nanoparticles underwent aggregation. With prolonged illumination, some flocculation occurred to yield a dark precipitate. In the absence of illumination, no spectral changes or flocculation occurred for at least one month (Figure S2a of the Supporting Information). Colloidal dispersions of TOAB-capped gold nanoparticles were illuminated under identical conditions. Absorption spectra were unchanged (Figure S2b), and no flocculation was observed.

XPS spectra were acquired for unilluminated and illuminated samples of 9-anthracenethiolate-capped gold nanoparticles (Figure S3 of the Supporting Information). The S 2p region of the spectra of both samples contained a peak centered at 163 eV, consistent with previously reported XPS spectra for gold-adsorbed alkanethiolates and arylthiolates.[62−66] Illumination did not cause significant changes of the XPS spectrum.

Gold colloids were characterized further by TEM. Unilluminated suspensions of 9-anthracenethiolate-capped gold nanoparticles consisted predominantly of isolated nanoparticles with average diameter of (15 ± 7) nm, as calculated by analysis of 40 particles using ImageJ software. (The polydispersity of samples was not deemed problematic for proof-of-concept experiments in materials assembly.) Illumination into the $\pi-\pi^*$ bands of 9-anthracenethiolate yielded aggregates of nanoparticles. Representative images are shown in Figure 2 for aliquots removed from a colloidal dispersion at illumination times from 0 to 45 h at 385 nm and 410 μW/cm^2. Aggregates with diameters up to 600 nm formed after 45 h of illumination. The average size of

(51) Kreibig, U.; Genzel, L. *Surf. Sci.* **1985**, *156*, 678–700.
(52) Dusemond, B.; Hoffmann, A.; Salzmann, T.; Kreibig, U.; Schmid, G. *Z. Phys. D: At., Mol. Clusters* **1991**, *20*, 305–308.
(53) Yang, W.-H.; Schatz, G. C.; Van Duyne, R. P. *J. Chem. Phys.* **1995**, *103*, 869–875.
(54) Weisbecker, C. S.; Merritt, M. V.; Whitesides, G. M. *Langmuir* **1996**, *12*, 3763–3772.
(55) Mayya, K. S.; Patil, V.; Sastry, M. *Langmuir* **1997**, *13*, 3944–3947.
(56) Brust, M.; Bethell, D.; Schiffrin, D. J.; Kiely, C. *J. Adv. Mater.* **1995**, *7*, 795–797.
(57) Elghanian, R.; Storhorr, J. J.; Mucic, R. C.; Letsinger, R. L.; Mirkin, C. A. *Science* **1997**, *277*, 1078–1081.
(58) Storhoff, J. J.; Elghanian, R.; Mucic, R. C.; Mirkin, C. A.; Letsinger, R. L. *J. Am. Chem. Soc.* **1998**, *120*, 1959–1964.
(59) Sastry, M.; Lala, N.; Patil, V.; Chavan, S. P.; Chittiboyina, A. G. *Langmuir* **1998**, *14*, 4138–4142.
(60) Thanh, N. T. K.; Rozenweig, Z. *Anal. Chem.* **2002**, *74*, 1624–1628.
(61) Aslan, K.; Luhrs, C. C.; Pérez-Luna, V. H. *J. Phys. Chem. B* **2004**, *108*, 15631–15639.
(62) Laibinis, P. E.; Whitesides, G. M.; Allara, D. L.; Tao, Y.-T.; Parikh, A. N.; Nuzzo, R. G. *J. Am. Chem. Soc.* **1991**, *113*, 7152–7167.
(63) Tarlov, M. J.; Burgess, J.; Donald, R. F.; Gillen, G. *J. Am. Chem. Soc.* **1993**, *115*, 5305–5306.
(64) Zharnikov, M.; Grunze, M. *J. Phys.: Condens. Matter* **2001**, *13*, 11333–11365.
(65) Heister, K.; Zharnikov, M.; Grunze, M.; Johansson, L. S. O. *J. Phys. Chem. B* **2001**, *105*, 4058–4061.
(66) Ballav, N.; Weidner, T.; Zharnikov, M. *J. Phys. Chem. C* **2007**, *111*, 12002–12010.

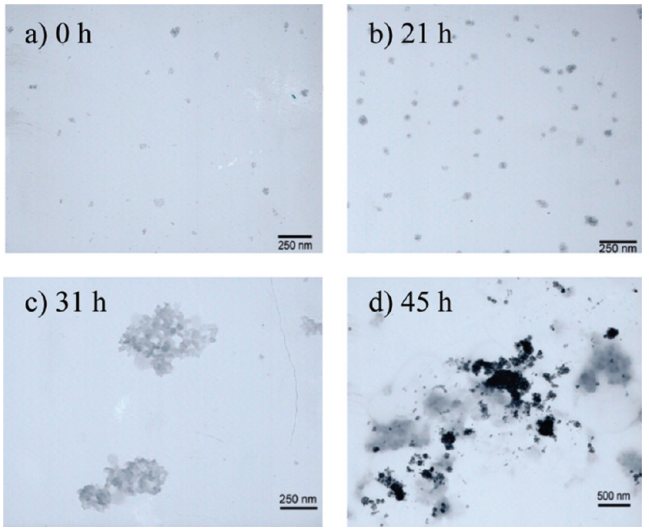

Figure 2. TEM images of 9-anthracenethiolate-capped gold nanoparticles from toluene suspensions illuminated for 0 (a), 21 (b), 31 (c), and 45 (d) h at 385 nm and 410 μW/cm^2.

aggregates and the density of nanoparticles within aggregates increased with illumination time. TEM images were also acquired for illuminated dispersions of TOAB-capped gold nanoparticles (Figure S4 of the Supporting Information). Little or no aggregation was observed after two days of illumination at 385 nm and 410 μW/cm^2. The rate of photoinduced aggregation of 9-anthracenethiolate-capped gold nanoparticles increased with illumination intensity. Representative TEM images are shown in Figure S5 for samples illuminated at 355 nm and 130 mW/cm^2. Aggregates with dimensions of several micrometers formed within 45 min of illumination. High-resolution TEM images revealed that the aggregates consisted of discrete gold nanoparticles, the lattice planes of which were oriented randomly (Figure S6).

Taken together, the absorption spectra, XPS spectra, and TEM images are consistent with a mechanism in which photodimerization reactions between adsorbed 9-anthracenethiolates caused the aggregation of gold nanoparticles. Importantly, the XPS spectrum of the illuminated sample exhibited negligible intensity at 167−168 eV, which would correspond to the S 2p peak of sulfonates.[62,63,67−69] The absence of such a peak reveals that the direct photooxidation of thiolates to sulfonates, which can be induced by UV illumination of thiolate-functionalized gold surfaces,[63,66,67,70−72] did not contribute significantly to the observed photochemistry. The lack of fusion of nanoparticles into larger crystallites provides additional evidence that alternative photochemical processes were not responsible for the observed aggregation of nanoparticles. Similarly, the lack of aggregation of illuminated TOAB-capped gold nanoparticles indicates that optical forces, charge-transfer reactions, or photothermal effects caused by excitation of the surface plasmon resonance or interband transitions of gold nanoparticles did not contribute significantly to aggregation. Finally, the lack of aggregation of unilluminated 9-anthracenethiolate-capped gold nanoparticles indicates that nonphotochemical interactions, such as dispersion forces between adsorbed anthryl groups, played a minimal role.

Two photodimerization reactions are possible: (1) *intramonolayer* photodimerization between anthryl groups adsorbed to the same gold nanoparticle and (2) *interfacial* photodimerization between anthryl groups adsorbed to different gold nanoparticles. To distinguish between the two mechanisms, we investigated the concentration dependence of the photoinduced aggregation of gold nanoparticles. Two dispersions of 9-anthracenethiolate-capped gold nanoparticles in toluene were illuminated at 355 nm and 70 mW/cm^2. Sample 1 consisted of the stock concentration of gold nanoparticles in a 0.2-cm cuvet; sample 2 consisted of a 1:5 dilution from the stock concentration in a 1.0-cm cuvet. Prior to illumination, the measured absorbances of the two samples were equal (Figure S7 of the Supporting Information). Illumination caused the anthryl $\pi-\pi^*$ absorbance (centered at 344 nm) of sample 1 to decrease more rapidly than that of sample 2 (Figure S7). If intramonolayer photodimerization were the only active mechanism, then the anthryl $\pi-\pi^*$ absorbances would have decreased with identical rates, because the surface coverage of 9-anthracenethiolate on gold nanoparticles was equal in the two samples. Alternatively, the rate of interfacial photodimerization should depend on the concentration of gold nanoparticles. Thus, the more rapid decrease of the anthryl $\pi-\pi^*$ absorbance for sample 1 clearly indicates that the interfacial photodimerization mechanism was active. The plasmon band of nonaggregated gold nanoparticles (530 nm) also decreased more rapidly for sample 1 than for sample 2 (Figure S7). The low-energy plasmon band beyond 640 nm, corresponding to aggregated gold nanoparticles, initially increased more rapidly for sample 1 than for sample 2. The band then decreased upon flocculation of nanoparticles. These illumination-induced changes of the plasmon bands indicate that the aggregation of gold nanoparticles was correlated with interfacial photodimerization.

Zhou et al. reported that intramonolayer photodimerization between adsorbed thymine derivatives led to the flocculation of aqueous gold colloids.[15] They attributed the effect to the increased hydrophobicity of nanoparticle surfaces upon dimerization of thymine. Such a mechanism is unlikely to contribute to the photodimerization-induced aggregation of 9-anthracenethiolate-capped gold nanoparticles. Dimerization through [4 + 4] cycloaddition should not change significantly the polarity of the anthryl group or the solvation of the nanoparticles by toluene. We conclude that interfacial photodimerization,

(67) Huang, J.; Hemminger, J. C. *J. Am. Chem. Soc.* **1993**, *115*, 3342–3343.
(68) Hutt, D. A.; Cooper, E.; Leggett, G. J. *J. Phys. Chem. B* **1998**, *102*, 174–184.
(69) Wang, M.-C.; Liao, J.-D.; Weng, C.-C.; Klauser, R.; Shaporenko, A.; Grunze, M.; Zharnikov, M. *Langmuir* **2003**, *19*, 9774–9780.
(70) Huang, J.; Dahlgren, D. A.; Hemminger, J. C. *Langmuir* **1994**, *10*, 626–628.
(71) Hutt, D. A.; Leggett, G. J. *J. Phys. Chem.* **1996**, *100*, 6657–6662.
(72) Leggett, G. J. *Chem. Soc. Rev.* **2006**, *35*, 1150–1161.

and the resulting formation of covalent linkages between 9-anthracenethiolate-capped gold nanoparticles, played a predominant role in the photoinduced aggregation mechanism.

Dimeric anthracene can be dissociated thermally or photochemically.[38] To investigate whether the photoinduced aggregation of gold nanoparticles was reversible, we illuminated into the blue-shifted $\pi-\pi^*$ bands of the anthracene dimer. A toluene dispersion of 9-anthracenethiolate-capped gold nanoparticles was first illuminated at 385 nm (410 μW/cm^2, 4 h) to induce aggregation, then at 285 nm (< 100 μW/cm^2, 1−4 h) to induce the photocycloreversion of the anthracene dimer.[38] Illumination at 385 nm resulted in a red-shift of the plasmon maximum from 529 to 555 nm (Figure S8 of the Supporting Information). A portion of the gold colloid flocculated irreversibly. Subsequent illumination at 285 nm caused a gradual blue-shift of the plasmon maximum from 555 to 533 nm. The long-wavelength tail of the plasmon band remained more intense than for the original sample, prior to illumination at 385 nm. (Residual aggregates in suspension presumably gave rise to both a long-wavelength plasmon band and a scattering-induced increase of the apparent baseline.) Nonetheless, the observed blue-shift of the plasmon maximum caused by illumination at 285 nm provides strong evidence that the photocycloreversion of anthracene resulted in the dissociation of aggregates of gold nanoparticles. Thus, the assembly of materials via the photodimerization of adsorbed anthryl derivatives is, in principle, reversible.

Photochemically Triggered Attachment of Gold Nanoparticles to ZrO_2 Surfaces. The attachment of gold nanoparticles to nanocrystalline ZrO_2 films was characterized as a prototypical example of photodimerization-induced materials assembly on surfaces. ZrO_2 was chosen for its 5.0-eV bandgap,[73,74] corresponding to an absorption onset of approximately 250 nm. The bandgap absorption of ZrO_2 does not interfere with the $\pi-\pi^*$ bands of anthracene, enabling selective excitation of anthryl groups during photoinduced materials assembly. SEM images revealed that the nanocrystalline ZrO_2 films were approximately 3 μm thick and consisted of roughly spherical aggregates of nanoparticles (Figure S9 of the Supporting Information). The average diameter of the aggregates was 35 ± 6 nm, as calculated by analysis of 46 aggregates using ImageJ software. Individual particles were resolvable within aggregates, but the resolution of our instrument was not sufficient to determine their size. The high surface area of nanocrystalline ZrO_2 films is advantageous for maximizing the surface loading of gold nanoparticles.

9-Anthroic acid and 2-anthroic acid were adsorbed to ZrO_2 films from THF. The $\pi-\pi^*$ bands were unshifted upon adsorption (Figure 3). The vibrational structure of the $\pi-\pi^*$ bands of 2-anthroic acid was less well-resolved after adsorption, whereas the vibrational structure for 9-anthroic acid was relatively unperturbed. Equilibrium binding data were modeled by the Langmuir adsorption isotherm (Figure S10 of the Supporting Information).[75] The surface adduct formation constants (K_{ad}) for 2- and 9-anthroic acid were (3.7 ± 0.6) × 10^3 and (3 ± 3) × 10^4 M^{-1}, respectively. (The relatively large standard deviations arise from the small y-intercepts of the Langmuir plots in Figure S10, from which K_{ad} values were extracted.) The saturation surface amounts per projected area (Γ_0) were (1.9 ± 0.1) × 10^{-7} and (5.4 ± 0.1) × 10^{-8} mol/cm^2 for 2- and 9-anthroic acid, respectively. Maximum coverages were attained after 6 h of immersion in THF solutions with concentrations greater than 1 mM. Coverages on the order of 10^{-7} mol/cm^2 are consistent with the adsorption of alkanoic and mercaptoalkanoic acids, porphyrins, and ruthenium polypyridyl complexes to nanocrystalline metal oxide films.[76−80] Anthracene exhibited negligible adsorption to ZrO_2 (Figure 3), indicating that 2- and 9-anthroic acid adsorbed through the carboxylic acid groups.

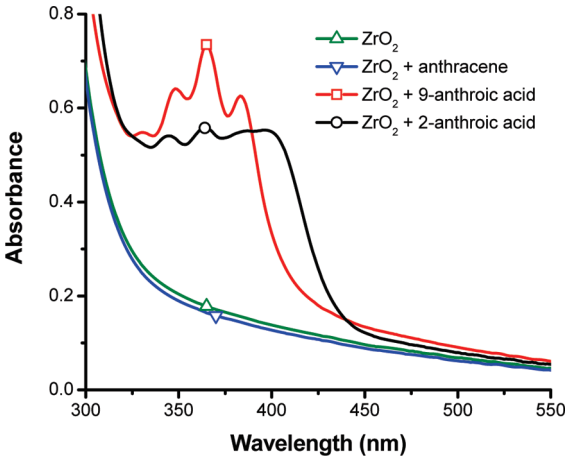

Figure 3. UV/vis absorption spectra of nanocrystalline ZrO_2 films after immersion in 15-mM THF solutions of anthracene, 9-anthroic acid, and 2-anthroic acid. Also shown is the spectrum of an unmodified ZrO_2 film.

IR spectra of ZrO_2 powders that were stirred in solutions of 9-anthroic acid and 2-anthroic acid were compared with those of free 9-anthroic acid, 2-anthroic acid, and the sodium salt of 9-anthroate in KBr matrices (Figure S11 of the Supporting Information). The 1680-cm^{-1} bands of free 9- and 2-anthroic acids were assigned to the asymmetric carboxylic acid stretching ($\nu_a(CO_2H)$) modes, on the basis of literature spectra of alkanoic acids.[81,82] For 9-anthroic acid, this band shifted to 1539 cm^{-1} upon adsorption to ZrO_2, consistent with deprotonation

(73) Sayama, K.; Arakawa, H. *J. Phys. Chem.* **1993**, *97*, 531–533.
(74) Sayama, K.; Arakawa, H. *J. Photochem. Photobiol., A* **1996**, *94*, 67–76.
(75) Langmuir, I. *J. Am. Chem. Soc.* **1918**, *40*, 1361–1402.
(76) Mann, J. R.; Watson, D. F. *Langmuir* **2007**, *23*, 10924–10928.
(77) Watson, D. F.; Marton, A.; Stux, A. M.; Meyer, G. J. *J. Phys. Chem. B* **2004**, *108*, 11680–11688.
(78) Obare, S. O.; Ito, T.; Meyer, G. J. *Environ. Sci. Technol.* **2005**, *39*, 6266–6272.
(79) Onozawa-Komatsuzaki, N.; Kitao, O.; Yanagida, M.; Himeda, Y.; Sugihara, H.; Kasuga, K. *New J. Chem.* **2006**, *30*, 689–697.
(80) Soja, G. R.; Mann, J. R.; Watson, D. F. *Langmuir* **2008**, *24*, 5249–5252.
(81) Hayashi, S.; Umemura, J. *J. Chem. Phys.* **1975**, *63*, 1732–1740.
(82) Allara, D. L.; Nuzzo, R. G. *Langmuir* **1985**, *1*, 52–66.

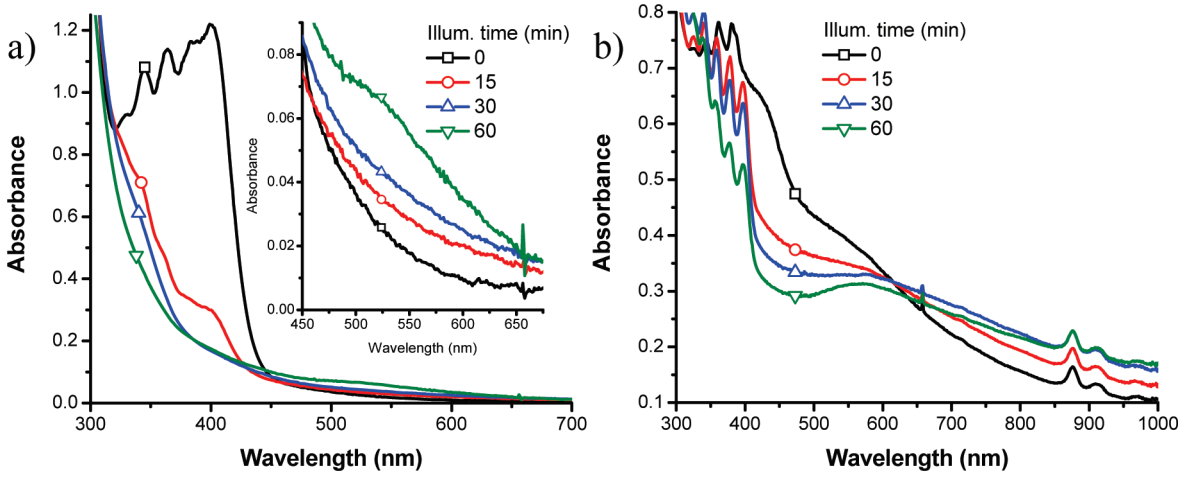

Figure 4. (a) UV/vis absorption spectra of 2-anthroate-functionalized ZrO_2 films immersed in toluene suspensions of 9-anthracenethiolate-capped gold nanoparticles and illuminated at 355 nm and 135 mW/cm^2. (inset) Absorption spectra from 450 to 650 nm. (b) UV/vis/NIR absorption spectra of suspensions of 9-anthracenethiolate-capped gold nanoparticles from the same experiment.

upon surface attachment.[82,83] Similarly, the $\nu_a(CO_2H)$ band of 2-anthroic acid shifted into a broad absorption centered at approximately 1540 cm^{-1}. (The bands at 1625 cm^{-1} in the spectra of ZrO_2 films functionalized with 9- and 2-anthroate are assigned to the bending mode of adsorbed water.[84]) The asymmetric carboxylate stretching ($\nu_a(CO_2^-)$) frequencies of ZrO_2-adsorbed 9- and 2-anthroate were approximately 20 cm^{-1} lower than that of the sodium salt of 9-anthroate, indicating that carboxylate groups were coordinated to surface Zr^{4+} sites.[85,86] The breadth of the $\nu_a(CO_2^-)$ bands and the symmetric carboxylate stretching ($\nu_s(CO_2^-)$) bands at 1390 cm^{-1} suggests that surface attachment occurred through multiple coordination modes.[85,86] The bands at 1487, 1433, 1320, and 1277 cm^{-1} were assigned as fundamental modes of the anthryl group, on the basis of previously reported spectra of anthracene.[87−89]

Before characterizing the photochemically triggered adsorption of nanoparticles to surfaces, we investigated intramonolayer photodimerization reactions of 2- and 9-anthroate adsorbed to ZrO_2. All photochemical experiments were performed on full monolayers with saturation surface amounts of 2- or 9-anthroate per projected area. Films were immersed in neat toluene and illuminated with 355 nm light at 50 mW/cm^2. (In the absence of illumination, 2- and 9-anthroate exhibited negligible desorption into toluene for at least 20 h.) For both 2- and 9-anthroate on ZrO_2, illumination caused a decrease of the absorbance of the $\pi-\pi^*$ bands (Figure S12 of the Supporting Information). The spectral changes suggest that adsorbed anthroates underwent photodimerization through [4 + 4] cycloaddition. Decreased conjugation shifts the $\pi-\pi^*$ bands of dimerized anthracene to shorter wavelengths than those of monomeric anthracene.[38] Blue-shifted $\pi-\pi^*$ bands were not resolvable in the spectra of illuminated anthroate-functionalized ZrO_2 films, due to the onset of absorption from ZrO_2. Nonetheless, the decreased $\pi-\pi^*$ absorbance in the absence of dark desorption provides evidence for photodimerization. The photodimerization of 9-anthroate was slightly faster than that of 2-anthroate under identical conditions (Figure S12). The orientation of the anthryl groups relative to the surface may have influenced the intramonolayer photodimerization reactivity. For 9-anthroate, the base of the anthryl group, or the line defined by carbons 1, 9, and 8, was probably constrained to the plane of the ZrO_2 surface, which may have promoted a favorable geometry for intramonolayer photodimerization.

2-Anthroate-functionalized ZrO_2 films were used as substrates for the photodimerization-induced adsorption of gold nanoparticles. We reasoned that the slower intramonolayer photodimerization of 2-anthroate relative to 9-anthroate would promote more efficient *interfacial* photodimerization. 2-Anthroate-functionalized ZrO_2 films were immersed in toluene suspensions of 9-anthracenethiolate-capped gold nanoparticles and were illuminated at 355 nm and 135 mW/cm^2. The progress of each reaction was monitored by acquiring UV/vis/NIR absorption spectra of the ZrO_2 film and the surrounding suspension of gold nanoparticles. ZrO_2 films were removed from suspension and rinsed with toluene prior to the acquisition of absorption spectra. Dilute gold colloids were used for initial mechanistic experiments, such that gold plasmon bands of suspensions were onscale in 1-cm cuvets. As a result of illumination, the absorption spectra of 2-anthroate-functionalized ZrO_2 films exhibited a decrease of the anthryl $\pi-\pi^*$ absorbance and the growth of a broad band centered at 530 nm (Figure 4a), corresponding to the surface plasmon band of gold nanoparticles. The films turned visibly red (Figure S13a of the Supporting Information). The growth of the plasmon band and the red coloration provide evidence for the

(83) Arnold, R.; Azzam, W.; Terfort, A.; Wöll, C. *Langmuir* **2002**, *18*, 3980–3992.
(84) Connor, P. A.; Dobson, K. D.; McQuillan, A. J. *Langmuir* **1999**, *15*, 2402–2408.
(85) Deacon, G. B.; Phillips, R. J. *Coord. Chem. Rev.* **1980**, *33*, 227–250.
(86) Nakamoto, K. *Infrared and Raman Spectra of Inorganic and Coordination Compounds*, 5th ed.; John Wiley and Sons: New York, 1997.
(87) Califano, S. *J. Chem. Phys.* **1962**, *36*, 903–909.
(88) Bree, A.; Kydd, R. A. *J. Chem. Phys.* **1968**, *48*, 5319–5325.
(89) Cané, E.; Miani, A.; Palmieri, P.; Tarroni, R.; Trombetti, A. *J. Chem. Phys.* **1997**, *106*, 9004–9012.

photoinduced attachment of gold nanoparticles to ZrO_2. (The plasmon band of the surrounding suspension of gold nanoparticles decreased in intensity, broadened, and red-shifted (Figure 4b), suggesting that gold nanoparticles aggregated in suspension.[51−53]) SEM images (Figure S9c) revealed that the average size of the aggregates within ZrO_2 films increased from 35 ± 6 to 41 ± 9 nm upon photoinduced attachment of 9-anthracenethiolate-capped gold nanoparticles to the surface. The morphology of ZrO_2 was unchanged upon adsorption of 2-anthroate. Individual gold nanoparticles were not resolvable; thus, we were unable to determine whether gold nanoparticles were present in partial monolayers, full monolayers, or multilayers.

Three control experiments were performed to further investigate the mechanism of photoinduced attachment of gold nanoparticles to ZrO_2. In the first experiment, 2-anthroate-functionalized ZrO_2 films were immersed in suspensions of 9-anthracenethiolate-capped gold nanoparticles without illumination. The absorbance of these films at 530 nm increased minimally, but at a much slower rate than for illuminated films (Figure S14a of the Supporting Information). We attribute the slight increase of absorbance to the physisorption of gold nanoparticles to ZrO_2, perhaps driven by dispersion forces between adsorbed anthryl groups. No visible color change was observed on the films (Figure S13b). The intensity of the plasmon band of the surrounding gold suspension decreased slightly but did not broaden or shift to longer wavelengths (Figure S14b). (The decreased intensity probably arose from the removal of gold nanoparticles from suspension through physisorption to ZrO_2 and/or flocculation.) In the second control experiment, unfunctionalized ZrO_2 films were immersed in toluene suspensions of 9-anthracenethiolate-capped gold nanoparticles and illuminated at 355 nm and 135 mW/cm^2. Negligible changes were observed in the absorption spectrum of the ZrO_2 film, indicating that little or no attachment of gold nanoparticles occurred. Finally, 2-anthroate-functionalized ZrO_2 films were immersed in toluene suspensions of octanethiolate-capped gold nanoparticles and were illuminated at 355 nm and 135 mW/cm^2. The $\pi-\pi^*$ absorbance of 2-anthroate decreased with illumination, but the absorbance at 530 nm did not increase (Figure S15a). The color of the ZrO_2 films (Figure S13c) and the absorption spectra of the surrounding suspension of gold nanoparticles (Figure S15b) were essentially unchanged. These control experiments reveal that little or no adsorption of gold nanoparticles occurred unless each of the following conditions was satisfied: (1) gold nanoparticles were functionalized with 9-anthracenethiolate, (2) ZrO_2 films were functionalized with 2-anthroate, and (3) the $\pi-\pi^*$ transition of anthryl groups was excited.

Notably, the $\pi-\pi^*$ absorbance of ZrO_2-adsorbed 2-anthroate decreased more rapidly in the presence of 9-anthracenethiolate-capped gold nanoparticles than in the presence of octanethiolate-capped gold nanoparticles (Figures 4 and S15 of the Supporting Information). The rates of intramonolayer photodimerization on ZrO_2 were presumably equal for the two experiments; therefore, the faster spectral changes in the presence of 9-anthracenethiolate-capped gold nanoparticles arose from an additional pathway, which we attribute to interfacial photodimerization. The photochemistry involved in the reaction mixtures was undoubtedly complex, and any of the following photodimerization reactions may have contributed to the observed spectral changes: (1) intramonolayer photodimerization between 9-anthracenethiolates on gold, (2) intramonolayer photodimerization between 2-anthroates on ZrO_2, (3) interfacial photodimerization between 9-anthracenethiolates on different gold nanoparticles within the colloid, (4) interfacial photodimerization between 2-anthroates on ZrO_2 and 9-anthracenethiolates on gold, and (5) interfacial photodimerization between 9-anthracenethiolates on ZrO_2-adsorbed gold nanoparticles and 9-anthracenethiolates on suspended gold nanoparticles. The third reaction probably caused the observed aggregation of dispersed gold nanoparticles; however, these aggregates did not precipitate onto the surfaces of unfunctionalized ZrO_2 films in significant quantities. Therefore, the third reaction alone was not sufficient to cause the photoinduced attachment of gold nanoparticles to ZrO_2. The fifth reaction could lead to the deposition of multilayers of gold nanoparticles on ZrO_2 surfaces. In summary, despite the complexity of the reaction mixtures and the range of possible photodimerization reactions, the spectral data in Figure 4 and the results of control experiments provide compelling evidence that the attachment of 9-anthracenethiolate-capped gold nanoparticles to 2-anthroate-functionalized ZrO_2 films was driven by interfacial photodimerization reactions.

The rate of photoinduced attachment of gold nanoparticles to ZrO_2 surfaces increased with the concentration of gold colloids. In a representative experiment, 2-anthroate-functionalized ZrO_2 films were immersed in concentrated toluene suspensions of 9-anthracenethiolate-capped gold nanoparticles and were illuminated at 355 nm and 115 mW/cm^2. (The gold colloids were approximately 12 times more concentrated than those used in the mechanistic experiments described above; the absorbance at the plasmon band maximum was offscale.) Reaction progress was monitored by acquiring UV/vis/NIR absorption spectra of 2-anthroate-functionalized ZrO_2 films, which were removed from gold colloids and rinsed with toluene prior to spectral acquisition. Illumination caused the rapid diminution of the low-energy tail of anthryl $\pi-\pi^*$ bands and the growth of a broad gold plasmon band centered at 568 nm and extending beyond 1000 nm (Figure 5a). The plasmon band intensified with prolonged illumination, reaching an absorbance greater than 1 after 90 min. The films turned dark purple in color (Figure 5a, inset). In the absence of illumination, the anthryl $\pi-\pi^*$ absorbance decreased by approximately 0.1 over 60 min, but the absorbance beyond 400 nm did not change appreciably (Figure 5b). These results are consistent with the photochemically triggered attachment of gold nanoparticles to ZrO_2 through interfacial photodimerization between adsorbed anthryl groups. We were unable to determine the surface coverage of gold

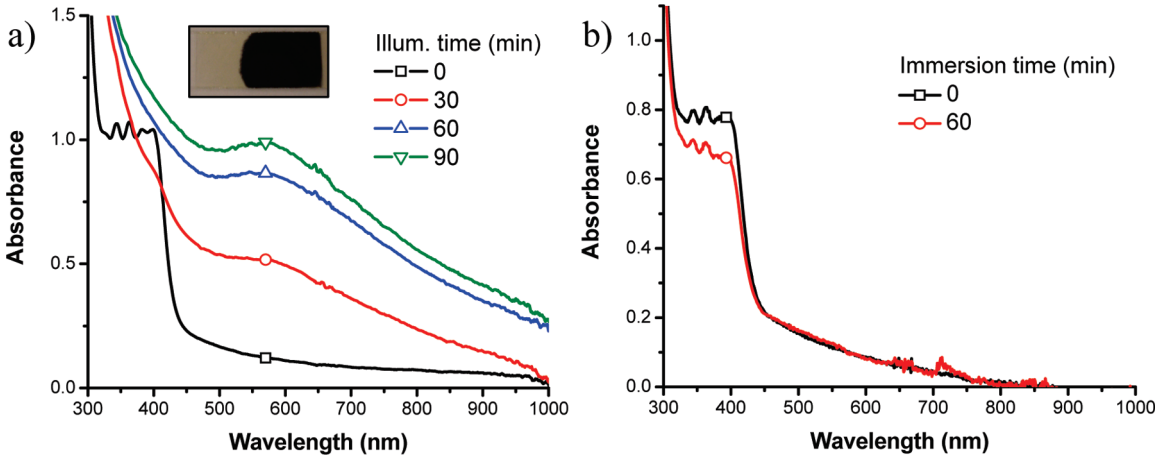

Figure 5. (a) UV/vis/NIR absorption spectra of 2-anthroate-functionalized ZrO_2 films immersed in toluene suspensions of 9-anthracenethiolate-capped gold nanoparticles and illuminated at 355 nm and 115 mW/cm^2 for varying times. (inset) Digital photograph of a 2-anthroate-functionalized ZrO_2 film, the right half of which was illuminated in the presence of 9-anthracenethiolate-capped gold nanoparticles. (b) UV/vis/NIR absorption spectra of 2-anthroate-functionalized ZrO_2 films immersed in toluene suspensions of 9-anthracenethiolate-capped gold nanoparticles in the absence of illumination.

nanoparticles from absorption spectra, because the extinction coefficient of the plasmon band of adsorbed nanoparticles was unknown. (Precise determination of the extinction coefficient is complicated by the spectral shifts associated with aggregation and adsorption of the nanoparticles.) Nonetheless, the increased concentration of gold colloids clearly caused a significant increase of the reaction rate, which is advantageous for applications in materials assembly.

ToF-SIMS data were acquired to further characterize the photochemical mechanism. Spectra were obtained for illuminated and unilluminated regions of a 2-anthroate-functionalized ZrO_2 film that was immersed in a toluene suspension of 9-anthracenethiolate-capped gold nanoparticles. (The concentration of gold and the illumination conditions were the same as for the absorption spectra in Figure 5.) The areas of the illuminated and unilluminated regions of the film were approximately 1.5 cm^2. ToF-SIMS data were acquired over 0.2-mm^2 areas within each region. To enable comparison of peak intensities for the two regions, both spectra were normalized to the total ion intensity.

The spectra of both regions contained gold-associated peaks, the most intense of which had the following masses (in Da) and assignments: 197.0 (Au^-), 393.9 (Au_2^-), and 590.9 (Au_3^-) (Figure S16 of the Supporting Information). The presence of gold-associated peaks in ToF-SIMS spectra confirms that the observed changes of color and absorption spectra arose from the attachment of gold nanoparticles to ZrO_2. The sum of the integrated normalized intensities of the peaks centered at 197.0, 393.9, and 590.9 Da was approximately 4.5 times greater for the illuminated region of the film than for the unilluminated region. Thus, illumination at 355 nm caused significantly increased coverage of gold nanoparticles on ZrO_2. The measurable intensity of gold-associated peaks for the unilluminated region suggests that some physisorption of gold nanoparticles occurred, consistent with the slight increase of the plasmonic absorption of substrates and the decrease of the plasmonic absorption of the surrounding suspension in the absence of illumination (Figure S14).

ToF-SIMS spectra contained weak molecular-ion peaks for 9-anthracenethiolate (209.0 Da, $C_{14}H_9S^-$) (Figure S17a of the Supporting Information), as well as the [4 + 4] cycloaddition products of interfacial photodimerization (430.9 Da, $C_{29}H_{18}SO_2^-$ and 432.0 Da, $C_{29}H_{19}SO_2^-$), intramonolayer photodimerization of 2-anthroate (442.9 Da, $C_{30}H_{19}O_2^-$), and intramonolayer photodimerization of 9-anthracenethiolate (419.0 Da, $C_{28}H_{19}S_2^-$ and 420.0 Da, $C_{28}H_{20}S_2^-$) (Figure S17b–d). The molecular-ion peak for 2-anthroate (221.0 Da, $C_{15}H_9O_2^-$) was poorly resolved (Figure S17e). (Peaks at masses above the nominal mass were assigned to organic fragments, whereas peaks at masses below the nominal mass were assigned to predominantly inorganic fragments. ToF-SIMS analysis of organic materials leads to significant fragmentation, as a result of the high energy impact of the primary ion; spectra of monolayer-functionalized ZrO_2 films contained peaks at all mass numbers. The m/z axis was calibrated using peaks assigned to inorganic ions; therefore, the apparent masses of peaks assigned to organic ions may be shifted slightly from their theoretical exact masses. The masses of peaks assigned to the organic fragments listed above were accurate within 0.3 Da of the theoretical values.) The peaks attributed to photodimerization products were 4- to 6-fold more intense for the illuminated region than for the unilluminated region; however, quantification of relative intensities was difficult, due to the low intensities of these peaks and the nonzero baseline intensity at all masses. Nonetheless, the ToF-SIMS data reveal that both interfacial and intramonolayer photodimerization reactions occurred in illuminated regions of the samples.

Peaks with higher masses and greater intensities also arose from interfacial photodimerization. The spectrum of the illuminated region of the substrate contained peaks with the following masses (in Da) and assignments (Figure 6): 733.8 ($^{90}ZrO_3C_{29}H_{19}SAu^-$), 734.8 ($^{90}ZrO_3C_{29}H_{20}SAu^-$, $^{91}ZrO_3C_{29}H_{19}SAu^-$), 735.8 ($^{90}ZrO_3C_{29}H_{21}SAu^-$, $^{91}ZrO_3C_{29}H_{20}SAu^-$, $^{92}ZrO_3C_{29}H_{19}SAu^-$), 736.8 ($^{90}ZrO_3C_{29}H_{22}SAu^-$, $^{91}ZrO_3C_{29}H_{21}SAu^-$, $^{92}ZrO_3C_{29}H_{20}SAu^-$),

737.8 ($^{91}ZrO_3C_{29}H_{22}SAu^-$, $^{92}ZrO_3C_{29}H_{21}SAu^-$, $^{94}ZrO_3C_{29}H_{19}SAu^-$), and 738.8 ($^{92}ZrO_3C_{29}H_{22}SAu^-$, $^{94}ZrO_3C_{29}H_{20}SAu^-$). The peak at 733.8 Da corresponds to the interfacial photodimerization product ($C_{29}H_{19}SO_2$) tethered to Au and ^{90}ZrO. The peaks at higher masses arise both from the heavier isotopes of Zr and from the addition of one, two, or three protons. The existence of fragments with different protonation states is supported by the relative intensities of the peaks. The ratios of the integrated normalized intensities of peaks at 733.8, 734.8, 735.8, and 737.8 Da in the spectrum of the illuminated region were approximately 5:3:5:3, which differs from the expected ratio of approximately 9:2:3:3 if these peaks arose only from the isotopic distribution of Zr. The presence of peaks at 736.8 and 738.8 Da provides further evidence that fragments with different protonation states were formed. (Peaks at 736.8 and 738.8 Da would otherwise correspond to $ZrO_3C_{29}H_{19}SAu^-$ with non-naturally occurring isotopes of ^{93}Zr and ^{95}Zr.) The sum of the integrated normalized intensities of the six peaks from 733.8 to 738.8 Da was approximately 26 times greater for the illuminated region than the unilluminated region of the substrate. The greater intensity of these peaks, which correspond to the interfacial photodimerization product tethered to both gold and ZrO_2, in the spectrum of the illuminated region of the film is consistent with a photochemical mechanism involving interfacial photodimerization.

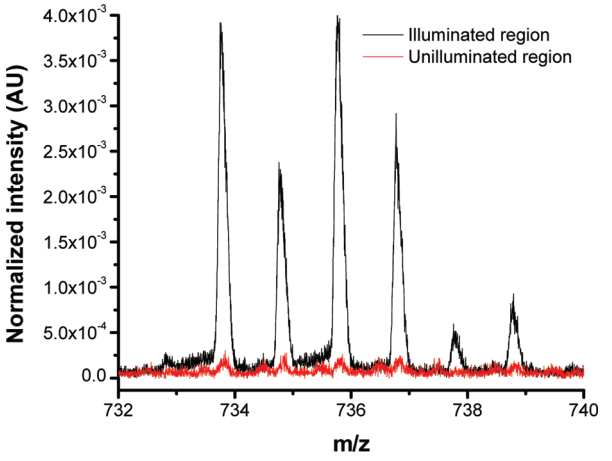

Figure 6. ToF-SIMS spectra for illuminated (355 nm, 115 mW/cm^2, 90 min) and unilluminated regions of a 2-anthroate-functionalized ZrO_2 film that was immersed in a suspension of 9-anthracenethiolate-functionalized gold nanoparticles. Peak assignments are discussed in the text.

To investigate whether the photodimerization-induced adsorption of gold nanoparticles to ZrO_2 was reversible, gold-functionalized ZrO_2 films were heated in air at 250 °C for 1 h. The gold plasmon band blue-shifted and narrowed with a maximum at 540 nm (Figure S18 of the Supporting Information). The band was similar to that of 9-anthracenethiolate-capped gold nanoparticles dispersed in toluene (Figure 1). We attribute the spectral changes to dissociation of the interfacial dimer and the corresponding decrease of electronic coupling between gold nanoparticles within the film. Thus, the thermally induced spectral changes provide further evidence that photoinduced materials assembly was driven primarily by interfacial photodimerization. We have not yet achieved reversible materials assembly on nanocrystalline surfaces. Thermally reversible assembly is precluded by the low boiling points of organic solvents in which 9-anthracenethiolate-capped gold nanoparticles are dispersible. Prolonged illumination of gold-functionalized ZrO_2 films, immersed in toluene, at 285 nm ($< 100\ \mu W/cm^2$) did not induce a measurable decrease of the amount of gold on the ZrO_2 surface. We speculate that extensive cross-linking and/or slow diffusion through the porous film may have prevented significant desorption of nanoparticles into the surrounding solvent.

Patterned Deposition of Nanoparticles onto Surfaces. Patterned arrays of 9-anthracenethiolate-capped gold nanoparticles were deposited onto 2-anthroate-functionalized ZrO_2 surfaces by illumination through a mask during the photodimerization reaction. Chemical images of the resulting micropatterned films were constructed from ToF-SIMS data (Figure 7). The images were normalized to the total ion intensity to account for any sample topography. An image constructed from the normalized sum of the intensities of peaks at 197.0 (Au^-), 393.9 (Au_2^-), and 590.9 Da (Au_3^-) reproduced the features of the photomask (Figure 7a). These gold-associated peaks were significantly more intense in illuminated regions of the film than in unilluminated regions, providing further evidence that excitation of anthryl

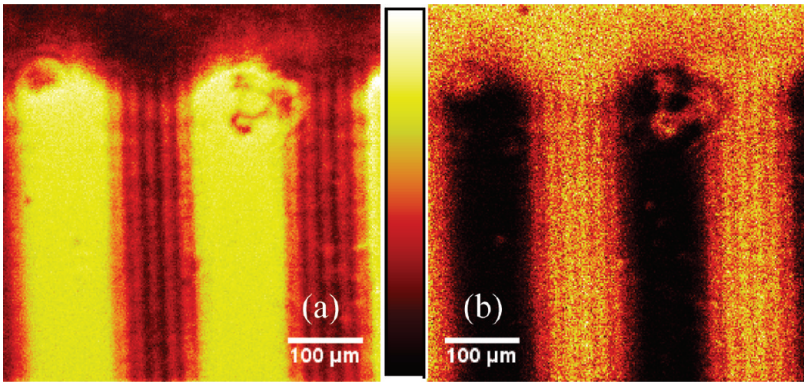

Figure 7. ToF-SIMS chemical images showing relative intensities of gold-associated (a) and ZrO_2-associated (b) peaks for a 2-anthroate-functionalized ZrO_2 film that was immersed in a suspension of 9-anthracenethiolate-capped gold nanoparticles and illuminated at 355 nm and 115 mW/cm^2. A scale bar is between the images.

$\pi-\pi^*$ transitions caused the attachment of gold nanoparticles to ZrO_2. The feature sizes of gold-containing regions were on the order of 100 μm, consistent with those of the mask. Fringe patterns were present within unilluminated regions of the ZrO_2 substrate. These presumably arose from diffraction of the incident light by the photomask. A second image was constructed from the normalized sum of the intensities of peaks at 121.9 ($^{90}ZrO_2^-$), 123.9 ($^{92}ZrO_2^-$), and 125.9 Da ($^{94}ZrO_2^-$) (Figure 7b). These ZrO_2-associated peaks were significantly less intense in illuminated, gold-coated regions of the film than in unilluminated regions. Both the generation and escape of substrate-associated ions were less efficient in gold-coated regions of the film.

Conclusions

We have reported the photochemically triggered assembly of gold nanoparticles in suspension and attachment of gold nanoparticles to ZrO_2 surfaces. In proof-of-concept experiments, micropatterned surfaces were prepared by illumination through a mask. The mechanism appears to involve the photoinduced interfacial [4 + 4] cycloaddition of adsorbed anthryl moieties. We have not yet optimized the photochemistry, and multiple interfacial and/or intramonolayer photodimerization reactions may play a role in or compete with materials assembly processes. Similarly, we have not precisely quantified the surface loading of gold nanoparticles on ZrO_2. Multilayer formation may have occurred under prolonged illumination. Ongoing research in our laboratory is directed toward optimizing the efficiency of interfacial photodimerization reactions, characterizing more precisely the composite materials prepared via this approach, and expanding the scope of this materials assembly method.

Photodimerization-induced materials assembly offers certain advantages over the aggregation or deposition of nanoparticles via optical forces or charge-transfer processes induced by direct excitation of nanoparticles: (1) our approach yields covalent linkages between nanoparticles or between nanoparticles and substrates, potentially enabling control over interfacial distance and electronic coupling; (2) our preliminary data suggest that materials assembly may be reversible through the photocycloreversion of the anthracene dimer; (3) because the photochemistry involves adsorbed functional groups rather than the nanoparticle itself, we anticipate (but have not yet demonstrated) that our approach will be applicable to the assembly of materials with widely varied compositions, sizes, and surface chemistries; (4) photodimerization-induced materials assembly occurs under low light intensities, at which aggregation induced by optical forces is immeasurably slow.

Finally, photodimerization-induced materials assembly may be an attractive alternative to hybrid top-down/bottom-up approaches for certain applications. Our approach combines photopatterning (top-down) and nanoparticle-adsorption (bottom-up) steps into a single photoinduced reaction, potentially streamlining materials assembly processes. Multicomponent nanostructured materials and ternary and higher-order patterned arrays of nanoparticles on surfaces may be accessible through this technique.

Acknowledgment. This work was funded by the National Science Foundation (CHE-0645678) and the University at Buffalo, State University of New York. We thank David Wells for his assistance in obtaining and interpreting ToF-SIMS data, Robyn Goacher for her assistance in interpreting XPS spectra, Prof. Joseph Gardella for the use of ToF-SIMS instrumentation, and Peter Bush for assistance in obtaining SEM images and XPS spectra.

Supporting Information Available: Mass spectrum of 9-anthracenethiolate, SEM images of nanocrystalline ZrO_2 films, equilibrium binding data and IR spectra for the adsorption of 2- and 9-anthroic acids to ZrO_2, TEM images and XPS spectra for 9-anthracenethiolate-capped gold nanoparticles, absorption spectra and TEM images for control experiments, photographs of gold-functionalized ZrO_2 films and unfunctionalized films from control experiments, and ToF-SIMS spectra. This material is available free of charge via the Internet at http://pubs.acs.org.